Global features of Kelvin-Helmholtz waves at the magnetopause for northward interplanetary magnetic field

Wenya Li,[1,2] Chi Wang,[1] Binbin Tang,[1] Xiaocheng Guo,[1] and Dong Lin[1,2]

[1]   We investigate the global features of Kelvin-Helmholtz waves (KHW) at the low-latitude magnetopause for constant northward interplanetary magnetic field conditions, using global magnetohydrodynamic simulations. The root-integrated power (*RIP*) of *X* component of bulk velocity is employed to analyze the magnetopause mode of KHW along the boundary layer. The *RIP* distribution of the outer KHW is much broader than that of the inner one, and the maximum amplitude of global KHW occurs near the dawn/dusk terminator regions. In the dayside magnetopause, the phase of the waveform at middle latitudes leads to that at low latitudes, while the situation reversed in the nightside. The global evolution of KHW phases is a representation of an interesting feature that the axis of the Kelvin-Helmholtz vortex aligns with the geomagnetic field lines. We suggest that the reported features may also exist in other KHW active regions with flow-sheared plasma.

Citation: Li, W., C. Wang, B. Tang, X. Guo, and D. Lin (2013), Global features of Kelvin-Helmholtz waves at the magnetopause for northward interplanetary magnetic field, *J. Geophys. Res. Space Physics*, *118*, doi:10.1002/jgra.50498.

1. Introduction

[2]   The boundary of two plasmas is Kelvin-Helmholtz unstable when there is enough velocity shear across the interface [*Chandrasekhar*, 1961]. The temporal growth rate γ of the Kelvin-Helmholtz waves (KHW) at the plasmas' boundary from the linear theoretical work, which is valid for incompressible plasmas separated by tangential discontinuity, is given by

$$\gamma = \sqrt{\frac{1}{m_i(n_1+n_2)}\left\{\frac{m_i n_1 n_2}{n_1+n_2}(\triangle\mathbf{V}\cdot\mathbf{k})^2 - \frac{1}{\mu_0}\left[(\mathbf{B}_1\cdot\mathbf{k})^2 + (\mathbf{B}_2\cdot\mathbf{k})^2\right]\right\}},$$

(1)

where m_i is the ion mass, n is the plasma number density, μ_0 is the magnetic permeability in vacuum, $\triangle\mathbf{V}$ is the relative velocity, $\mathbf{B}$ is the magnetic field, and subscripts, "1" and "2", denote the two plasmas, respectively. Equation (1) suggests a configuration of magnetic field perpendicular to a sufficient velocity shear for the KHW excitation.

[3]   The low-latitude boundary layer (LLBL) of Earth's magnetosphere consists of a tailward moving plasma, which has properties intermediate between those of magnetosphere and magnetosheath, and comprises a large section of the magnetopause boundary layer [*Sckopke et al.*, 1981; *Sonnerup*, 1980]. Many previous studies have indicated

that the KHW is prone to be excited at the LLBL [e.g., *Lee et al.*, 1981; *Walker*, 1981; *Miura*, 1992], especially for northward interplanetary magnetic field (IMF) conditions [*Miura*, 1995; *Hasegawa et al.*, 2006]. Nevertheless, the KHW plays an irreplaceable role in the mass, momentum, and energy transport from the solar wind into the magnetosphere during northward IMF, via the surface waves and the vortices [*Miura*, 1984; *Terasawa et al.*, 1997; *Hasegawa et al.*, 2004; *Lai and Lyu*, 2010].

[4]   Numerical simulations have been widely used to study the criterion and the temporal evolution of KHW at the LLBL. The localized models have investigated the effect of orientation of magnetosheath magnetic field [*Miura*, 1995; *Cowee et al.*, 2010], the critical marker of rolled-up Kelvin-Helmholtz (K-H) vortices [*Takagi et al.*, 2006], and the reconnection inside the vortices resulting in mass transport [*Nykyri and Otto*, 2001]. Those models are specific to the planes with the maximal growth rates, e.g., the equatorial plane under the pure northward IMF. It is rarely addressed of the extent of the KHW out of the fastest-growing planes, which will lead to a full quantitative understanding of the KHW related transport processes [e.g., *Pu and Kivelson*, 1983], and benefits the targeted observations of KHW [e.g., *Hwang et al.*, 2012].

[5]   *Farrugia et al.* [1998] presented one particular numerical work to study the KHW unstable region of the dayside magnetopause, which is demonstrated quantitatively with temporal growth rate. The dayside magnetopause boundary layer was found to be KHW active from low to middle latitudes, except for a 2 h local time band on either side of noon; however, the nightside magnetopause and spatial evolution picture are not considered. Moreover, the localized simulations have implied an interesting feature that the axis of the K-H vortex aligns with the magnetic field when the

---

[1]State Key Laboratory of Space Weather, Center for Space Science and Applied Research, Chinese Academy of Sciences, Beijing, China.
[2]University of the Chinese Academy of Sciences, Beijing, China.

Corresponding author: C. Wang, State Key Laboratory of Space Weather, Center for Space Science and Applied Research, Chinese Academy of Sciences, 1 Nanertiao, Zhongguancun, PO Box 8701, Beijing 100190, China. (cw@spaceweather.ac.cn)

angle between the sheared velocity and magnetic field are nearly 90° [*Miura*, 1995] and 120° [*Gratton et al.*, 2009], and this feature has not been fully realized during the spatial evolution of the global KHW.

[6] Most of the previous simulations of KHW are set in the rest frame of surface waves or vortices, and the periodic boundary conditions are used, with constant magnetosheath and magnetosphere background conditions. The KHW at the realistic magnetopause propagates convectively along the flank [*Mills et al.*, 2000], and the plasma parameters and magnetic field vary longitudinally and latitudinally. The global MHD model for studying the solar wind-magnetosphere-ionosphere system is a powerful tool to illustrate a continuous development of KHW from dayside to nightside magnetopause, and the realistic magnetopause shape, the plasma properties, and magnetic field geometry are taken into account [*Claudepierre et al.*, 2008; *Guo et al.*, 2010]. By using a global simulation model [*Hu et al.*, 2007], we have presented various results on the KHW during the northward IMF, including the characteristics and property of the two modes KHW along the outer and inner edges of the boundary layer, the spatial evolution stages classified from the perturbation power, the wave frequencies, wavelengths, and phase speeds under various solar wind speeds, and one comparison of the KHW frequencies on Earth's, Mercury's, and Saturn's magnetopauses [*Guo et al.*, 2010; *Li et al.*, 2012].

[7] As a natural extension of our previous works, this paper will investigate the global features of the KHW in the magnetopause boundary. We will study in detail the latitudinal extent of the KHW, the global KHW active region, and the spatial evolution feature. The KHW perturbation amplitude for quantitative analysis is represented by a physical parameter from a spectral analysis technique. The remainder of this paper is structured as follows: section 2 provides an introduction to the global MHD simulation model and the spectral analysis method. In section 3, we present the numerical results on global distribution of KHW perturbation power and global evolution of the wave phase. All the results are discussed in section 4, and section 5 summarizes the paper with a new schematic of KHW at magnetopause.

2. Methodology

2.1. Simulation Model

[8] The piecewise parabolic method (PPM) scheme of *Colella and Woodward* [1984] is a high-order extension of the Godunov's method [*Godunov*, 1959], which is a conservative numerical scheme for solving partial different equations. Similar to *Dai and Woodward* [1995], a PPM Lagrangian remap (PPMLR)-MHD algorithm was developed by *Hu et al.* [2007] for global modeling of the solar wind-magnetosphere-ionosphere system. This model has successfully reproduced the KHW in the LLBL during constant northward IMF conditions [*Guo et al.*, 2010] and standing shock waves in the middle- and high-latitude magnetosheath [*Guo et al.*, 2011].

[9] The model uses a Cartesian coordinate with the Earth's center at the origin and X, Y, and Z axes pointing to the Sun, dawn-dusk direction, and the north, respectively. Limited by the computer resource, the current KHW simulations employ a quarter solution domain, which is taken to be $-300\ R_E \le X \le 30\ R_E$, $0\ R_E \le Y, Z \le 150\ R_E$, and appropriate symmetry boundary conditions are used at the noon-midnight meridian ($Y = 0$) and the equator ($Z = 0$) [*Hu et al.*, 2007]. The quarter domain is divided into $450 \times 240 \times 240$ grid points with a minimal grid spacing of 0.1 R_E. An inner boundary of radius 3 R_E is set for the magnetosphere to avoid the complexity associated with the plasmasphere and large MHD characteristic velocity from the strong magnetic field.

[10] The Earth's magnetic field is approximated by a dipole field with a dipole moment of $8.06 \times 10^{22} A/m$ in magnitude. The solar wind parameters are $V_{X,SW} = -400, -600$, and -800 km/s in velocity, $n_{SW} = 5\ cm^{-3}$ in number density, and $T_{SW} = 0.91 \times 10^5\ K$ in temperature. The IMF is due northward with a magnitude of 5 nT. The initial state to start with is somewhat arbitrarily prescribed [*Hu et al.*, 2007]. In the region outside the inner boundary and on the left of $X = 15\ R_E$, the magnetic field is set to be the superposition of the Earth's dipole with a mirror dipole located at $(30, 0, 0)\ R_E$ and the initial plasma is static with spherically symmetrical distributions of density and pressure,

$$n = \text{MAX}\left(n_s\,(r/R_E)^{-3}, 0.2 n_{SW}\right),\ p = \text{MAX}\left(p_s\,(r/R_E)^{-2}, p_{SW}\right). \tag{2}$$

where $n_s = 10^4\ cm^{-3}$, $p_s = 4.18 \times 10^{-10}\ N/m^2$ and n_{SW} and p_{SW} are the solar wind number density and pressure, respectively. On the right of $X = 15 R_E$, a uniform solar wind and a uniform IMF B_Z are assumed.

[11] The solar wind dynamic and magnetic pressures are held constant in each simulation run; thus, any surface waves in the LLBL are not generated by magnetic reconnection near the subsolar point or pressure fluctuations of the solar wind. The KHW is sensitive to grid spacing, and a test run using $640 \times 360 \times 360$ grid points confirms the reliability of the numerical results [*Li et al.*, 2012]. The spatial distribution of KHW power in the equatorial plane are studied for the 400, 600, and 800 runs [*Li et al.*, 2012], and here we choose the case of 800 km/s as an example to illustrate the global features of KHW in detail.

2.2. Power Spectral Analysis Method

[12] The KHW has been fully developed after 4000 τ_A evolution from an initial state described above. We sample the following 4000 τ_A simulation data for the spectral analysis. Here τ_A is a normalized time unit and equals to be 0.935 s. To describe the distribution of KHW energy density in frequency space, we compute the power spectral density at each spatial point by *Paschmann and Daly* [1998]

$$P(f_n) = 2N\triangle t\,|F[n]|^2, \qquad n = 0, 1, \ldots, N/2 \tag{3}$$

where

$$F[n] = \frac{1}{N}\sum_{j=0}^{N-1} V_X[j] \exp\left[-\frac{2\pi i n j}{N}\right], \qquad n = 0, 1, \ldots, N-1 \tag{4}$$

and

$$f_n = \frac{n}{N\triangle t}, \qquad n = 0, 1, \ldots, N/2. \tag{5}$$

Here $\triangle t$ is the sampling rate, f_n are the discrete Fourier frequencies, N is the number of points in time series, and $F[n]$ is the discrete Fourier transform of the time series $V_X[j]$. For the study of KHW, these parameters are $\triangle t = 10\ \tau_A$ and $N = 400$; the corresponding highest resolvable frequency,

the Nyquist frequency, $f_{Ny} = 1/(2\triangle t) = 53.48$ mHz and the frequency resolution, $\triangle f = 1/(N\triangle t) = 0.27$ mHz. The V_X component, compared with other physical quantities, is best suited for the spectral analysis. A global picture of KHW is built by computing the root-integrated power (*RIP*) in an interested frequency band, [3, 15 mHz], via

$$RIP = \sqrt{\int_{f_a}^{f_b} P(f)\mathrm{d}f} \qquad (6)$$

which has unit of km/s in this study. The variable, *RIP*, has been used to describe magnetosphere perturbation by the solar wind dynamic pressure fluctuations [*Claudepierre et al.*, 2010]. The previous global simulation analysis reveals that the frequencies of KHW are from ∼5 mHz under 400 km/s V_{SW} to ∼10 mHz under 800 km/s V_{SW} [*Li et al.*, 2012]; therefore, the V_X *RIP* can be viewed as the perturbation amplitude of KHW from the Parseval's theorem:

$$\sqrt{\frac{1}{N}\sum_{j=0}^{N-1} V_X^2[j]} = \sqrt{\int_0^{f_{Ny}} P(f)\mathrm{d}f}. \qquad (7)$$

The perturbation amplitude (*RIP*) is computed from equation (6) by *MATLAB-pmtm* program, and this spectral estimation method is commonly referred to as the "multitaper method" [*Thomson*, 1982].

3. Numerical Results

3.1. KHW Perturbation Amplitude on Y-Z Plane

[13] In Figure 1, we plot the X component of the bulk velocity (V_X) in the equatorial plane for the case of 800 km/s V_{SW}, and two kinds of KHW fluctuations are observed through the color contours. *Lee et al.* [1981] have studied these two kinds of surface waves: one is excited at the magnetopause (outer mode) and the other is at the inner surface of the boundary layer (inner mode). The two modes are marked on the two sides of the boundary layer, as Figure 1 shows. Mostly, the outer mode is colored blue and the inner one is colored red. *Guo et al.* [2010] presented the characteristics of the inner and outer modes and found that the variants of the density and the magnetic field strength of the quasi-fast mode wave are in phase on the magnetosphere side, while they are out of phase on the magnetosheath side. The introduced spectral technique is adopted for further analysis of the two modes KHW by *Li et al.* [2012] and in this study.

[14] Figure 2a shows the spatial distribution of the root-integrated power (*RIP*) of V_X. The panel is a geocentric solar magnetospheric *Y-Z* plane cut at $X = 4$ R_E (dusk to the right). The labeled angle ($\theta = \arctan(Z/Y)$) in the black dashed line is viewed as "latitude", which is different from the latitude defined in a spherical coordinate. The distribution of V_X *RIP* is shown in filled color contours, with color scales from 25 to 75 km/s. The low bound of the scale is generally one third of the upper bound in the same plane to eliminate the background noise and to highlight the KHW perturbation amplitude. For the simulation runs of 400 and 600 km/s solar wind speeds, the *RIP* distributions, with smaller magnitudes, are similar to that displayed in Figure 2a. Two separate V_X *RIP* populations in Figure 2a illustrate the latitudinal extent of the inner and outer modes of KHW. The
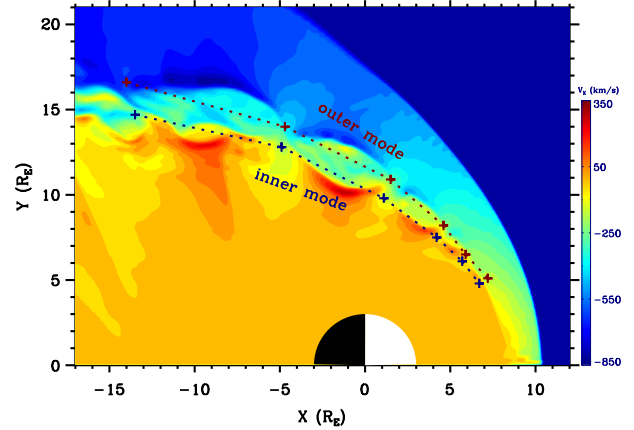
Figure 1. Equatorial cut of the Kelvin-Helmholtz waves under northward IMF. The outer and inner modes are illustrated generally by the red and blue dashed curves, respectively.

outer/magnetopause mode, represented by the outer populations, is KHW active with a large latitudinal extent. The latitudinal extent of the inner mode is much narrower and the KHW amplitude is weaker, which is generated by the latitudinal dissipation of velocity shear in the boundary layer. We pay close attention to the outer mode because the physical processes at the magnetopause are more pivotal for understanding of the solar wind transport into the magnetosphere [*Terasawa et al.*, 1997; *Nykyri and Otto*, 2001; *Hasegawa et al.*, 2004, 2009].

[15] The white curve in the left panel traces the V_X *RIP* peak from equator to middle latitude, and the magnetic tensor force is a probable factor to produce the latitudinal decrease of the KHW perturbation amplitude in the white curve. To clarify the stabilization effect of the magnetic field, the KHW linear criterion [*Chandrasekhar*, 1961] is checked with the plasma parameters and magnetic field near the magnetopause mode. Two black dash-dotted curves roughly indicate the locations of the magnetosheath (outer) and boundary layer (inner), respectively, and Figure 2b shows the profile between V_X *RIP* in the white curve and the corresponding magnetic shear angle. The magnetic shear angle, as a proxy for the temporal growth rate, is computed from the field direction difference of the two black dash-dotted curves. Three latitude angles ($\theta = 10°$, $20°$, and $30°$) are labeled in the right panel by the dashed lines.

[16] The KHW perturbation amplitude decreases linearly with the increase of the magnetic shear angle, and the KHW becomes negligible when the shear angle is larger than ∼ 30°, which is consistent with the quantitative estimation of dayside KHW unstable region by a 2-D numerical calculation [*Farrugia et al.*, 1998]. The temporal growth rate defined by equation (1) gives the same trend from the conditions of the two boundaries. The profiles of *RIP* and magnetic shear angle are similar in different *Y-Z* planes, while they are not always linear.

3.2. Global Distribution of KHW Amplitude

[17] The peak traces of perturbation amplitude of other 13 *Y-Z* cross sections are computed using the same method introduced in the previous subsection, and Figure 3 displays
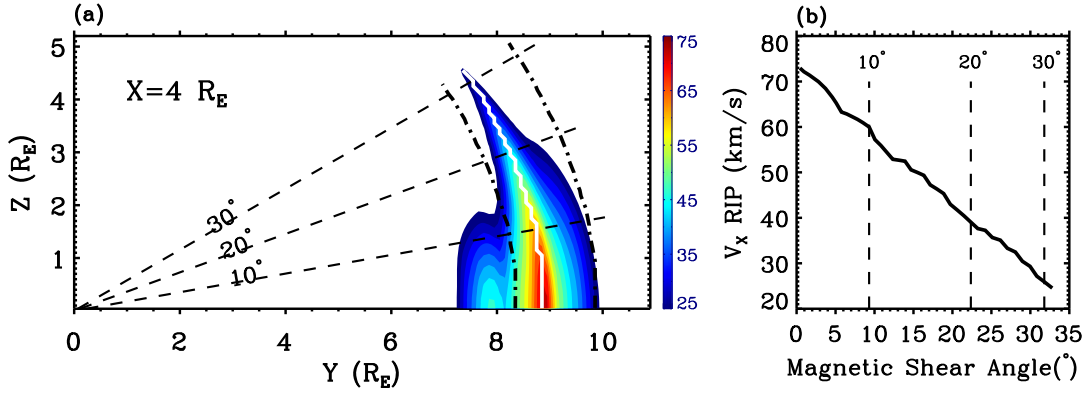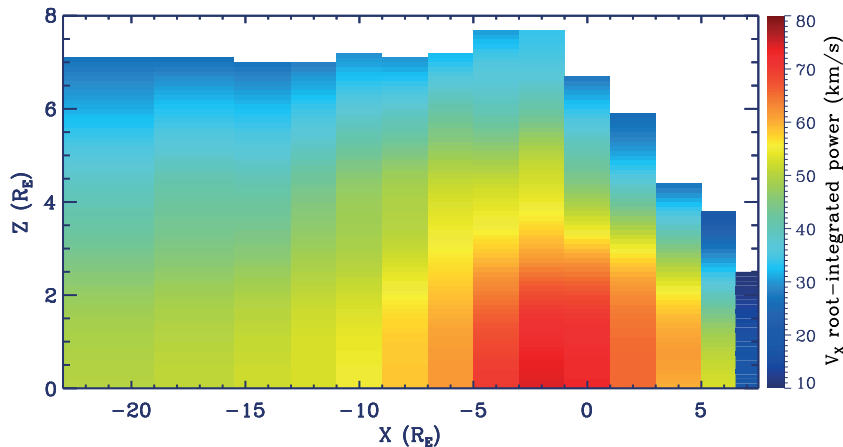
Figure 2. (a) Distribution of V_X root-integrated power (*RIP*) on the *Y-Z* plane with *X* position of 4 R_E and (b) the profile between V_X *RIP* in the white curve and magnetic shear angle around the magnetopause mode. In Figure 2a, the integrating frequency band is from 3 to 15 mHz [*Li et al.*, 2012] and the labeled angles from *arc tangent* of *Z/Y* illustrate the latitudinal change generally. The white curve tracks the *RIP* peak of the magnetopause mode from equator to middle latitude. In Figure 2b, the magnetic shear angle is computed from the magnetic field direction difference of the two black dash-dotted curves of Figure 2a, while the two curves represent the magnetosheath and boundary layer, respectively. The KHW perturbation amplitude decreases latitudinally by the increasing stabilization from the magnetic tensor force.

a global distribution of KHW fluctuations pieced together from 14 planes' peak traces. The vertical population at *X* = 4 R_E is from that in the white curve of Figure 2a. The V_X *RIP* distribution in Figure 3 represents a KHW active magnetopause marked with distinct perturbation amplitude. The distribution at *Z* = 0 R_E of Figure 3 illustrates V_X *RIP* in the equatorial plane, and the results are the square root of the magnetopause integrated power population [*Li et al.*, 2012]. The spatial evolution has been classified into four stages based on the power distribution: quasi-stable (not shown in Figure 3), exponential growth, linear growth, and nonlinear phases.

[18] In the dayside magnetopause, the V_X *RIP* increases continuously along the flank and the KHW active region broadens step by step along the latitude. The velocity shear in the dayside magnetopause increases gradually from the subsolar point to the magnetopause dawn/dusk flank region

[*Spreiter et al.*, 1966], and this generates effective destabilization to amplify the KHW. The developed KHW propagates and is gradually suppressed by the magnetic tension force when it reaches the middle latitudes, resulting in a latitudinally decreasing amplitude.

[19] The distinctive perpendicular configuration of the plasma flow and low-shear magnetic field produces the minimal stabilization effect of the magnetic field near regions of 06:00 and 18:00 h local times, which generates a maximal V_X *RIP* distribution around the dusk/dawn terminator as shown in Figure 3. It seems that the perturbation can extended to the highest latitude for the dawn/dusk region, and this is related with the local growth rate. The ladder-shaped distribution of KHW active region in the dayside magnetopause and its flank is consistent with the KHW unstable region for unambiguous temporal growth rates as obtained with boundary layer by *Farrugia et al.* [1998]

Figure 3. Global distribution of V_X root-integrated power (*RIP*) pieced together by peak traces of 14 planes. The vertical population at *X* = 4 R_E is from the distribution in the white curve of Figure 2. The *RIP* distribution demonstrates a KHW active ribbon with distinct fluctuation.

for pure northward IMF, while the active region from the distinct perturbation amplitude has a practical meaning for KHW detection and transport analysis.

[20] From the terminator to the nightside magnetopause, the width of the KHW active ribbon changes a little, while the saturated perturbation amplitude weakens progressively along the longitude. The vortex expands and the perturbation amplitude decreases, if we assume that the total energy of the vortex keeps nearly constant during the evolution. Besides, the KHW may be weakened by the decrease of the velocity shear between the boundary layer and magnetosheath and by the stabilization from the magnetic tensor force [*Takagi et al.*, 2006; *Cowee et al.*, 2010].

[21] To sum up, a global KHW active region is represented quantitatively with V_X *RIP*, whose distribution is described and explained in this subsection. One interesting thing is that the perturbation amplitude is strongest near the dusk/dawn terminator region, produced by one global perpendicular configuration of flow and magnetic fields. Tens of KHW observations were reported with Geotail/Cluster [*Hasegawa et al.*, 2006] and Double Star TC-1 [*Taylor et al.*, 2012] data under the quasi-northward IMF conditions, and a large portion of the cases were located in the KHW active ribbon demonstrated by Figure 3.

3.3. Global Evolution of KHW Phase

[22] Figure 4 shows V_X color contours in equatorial plane ($\theta = 0°$) and a rotated plane ($\theta = 30°$) along the X axis with an angle of 30° relative to the equator. Two vertical axes (R) are the radial distances from the X axis, and the step of the contours is 35 km/s. The magnetopause, illustrated by two black curves, are determined by the boundaries that divide the closed magnetospheric and open interplanetary magnetic field lines. The four waveforms in the upper panel are in their nonlinear evolution stage and the leading edges of the KHW are steeper than the trailing edges, consistent to the theory and prior observations of KHW [e.g., *Fairfield et al.*, 2000; *Hasegawa et al.*, 2009]. In the lower panel, the leading edges are also steeper than the trailing ones, while the KHW amplitude is smaller than that in the upper panel.

[23] Four red dots in the upper panel mark the positions of $|V_X|$ peak of each waveform. The velocities around the red dots exceed the corresponding velocities of magnetosheath and are associated with low plasma densities. These so-called lower-density and higher-speed features have been found in localized 3-D MHD simulation [*Takagi et al.*, 2006] and 2-D hybrid simulation [*Cowee et al.*, 2010] of KHW and have been used as one mark for identifying KHW cases in Geotail [*Hasegawa et al.*, 2006] and DOUBLE STAR TC-1 [*Taylor et al.*, 2012] observations.

[24] The $|V_X|$ peak positions displace gradually to the four corresponding red dots in the bottom panel of Figure 4 as θ increases from 0° to 30°. The peak location of the left-most waveform, taken as an example, exhibits a sunward displacement of $\sim 2.5\ R_E$, which is composed from the normal deformation of magnetopause [*Liu and Huang*, 2011] and displacement along the magnetopause. The displacement along the magnetopause denotes that the KHW phase in 30° θ plane is lagging behind that in the equator along the propagation direction of KHW in the LLBL. The magnitude of the lagging phase ($\triangle \phi$) is evaluated by a ratio of peak position displacement along the magnetopause to
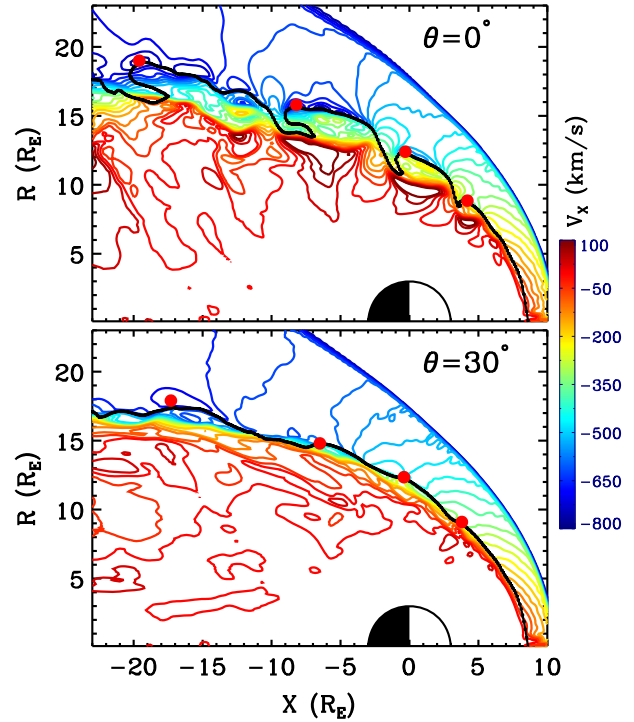

Figure 4. V_X color contours in the equatorial plane (upper panel) and one 30° rotated plane along the X axis relative to the equator (bottom panel). The vertical axes, R, are the radial distances from the X axis, and the range of the contours is from –800 to 100 km/s, with a contour step of 35 km/s. Two black curves illustrate the magnetopause boundaries by determining the boundaries that divide the closed magnetospheric and open interplanetary magnetic field lines. Four red dots in each panel represent the $|V_X|$ peak of four K-H waveforms.

local wavelength and that is $\sim -90°$ for the left-most waveform. The phase lagging feature is also unambiguous for the waveforms around $\sim -7\ R_E\ X$, and the displacement of the waveforms near the dusk terminator is inapparent.

[25] Figure 5 displays a snapshot of the right-most waveforms of Figure 4. One smaller contour step, 8.5 km/s, is set to highlight the distribution in the dayside, and the range is from –400 to 100 km/s. Similarly to Figure 4, two black curves illustrate the magnetopause boundary, and two red dots mark the $|V_X|$ peak positions of the waveforms. Unlike the sunward displacement of the two nightside waveforms, the red dot in the bottom panel of Figure 5 exhibits a duskward displacement compared to that in the equator. This indicates an interesting feature that the waveform in middle latitude is leading/prior to that in equator along the propagation direction of KHW. The magnitude of the displacement along the magnetopause ($\triangle d$) is $\sim 0.4\ R_E$, and the wavelength of the waveform is $\sim 3.5\ R_E$; therefore, the corresponding leading phase is $\sim 40°$. The grid spacing of $0.1R_E$ is accurate enough to identify the small displacement of the waveforms in the dayside.

[26] Figures 4 and 5 present examples of phase differences in two θ planes at one simulation time. We analyze the evolution of 300 τ_A in the same manner, with a time interval of 10 τ_A, and the differences of 15°, 20°, 25°, and 30° θ planes
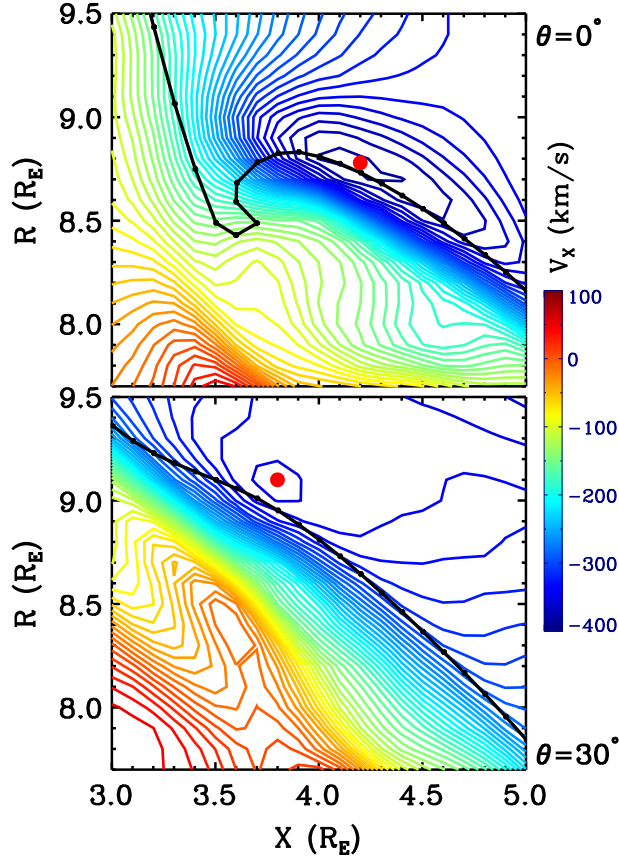
Figure 5. Snapshots of right-most waveforms in Figure 4. To highlight the two waveforms, the range of the color contours is set to be from −400 to 100 km/s, with a contour step of 8.5 km/s. Similarly to Figure 4, two red dots illustrate the $|V_X|$ peak in the two panels.

are calculated from dayside to nightside magnetopause. The results in 5° and 10° θ planes are not presented because the phase differences in the two planes are too small to identify, under the present grid spatial resolution.

[27] The method to compute the displacement along the magnetopause ($\triangle d$) follows the way of previous examples, and the phase difference ($\triangle\phi$) is the ratio of $\triangle d$ to local wavelength [*Li et al.*, 2012]. Figure 6 displays the distribution of $\triangle d$ (upper) and $\triangle\phi$ (bottom) along the X direction of four θ planes, and four colors, dark red, red, pale blue, and blue, distinguish the results of 30°, 25°, 20°, and 15° θ planes, respectively. Two dashed lines represent standard lines with zero displacement and zero phase difference in equatorial plane, respectively. The phase difference, or the displacement, is positive (negative) in the dayside (nightside) magnetopause, which indicates a phase leading (lagging) of middle latitude KHW, with the transition located near the dusk/dawn terminator. The distribution of Figure 6 demonstrates an interesting picture of KHW phase evolution from dayside to nightside magnetopause.

4. Discussion

[28] We have presented the global distribution of the KHW perturbation amplitude and the phase evolution.

Figure 7 shows a 3-D snapshot of one vortex in the night-side magnetopause boundary layer, with the X/Y position of $\sim -19/17$ R_E. The plasma number densities are displayed with filled color contours, in three X-Y planes with Z position of 0, 4, and 8 R_E, and the tangential bulk velocities are represented in red arrows. The coordinate is shifted to the KHW frame with a velocity of (−390, 130, 0 km/s). One black curve in each X-Y plane illustrates the magnetopause boundary by computing the open-closed magnetic field boundary. The vortex is distinguishable by the number density contours, the bulk flow arrows, and the magnetopause boundary. The geomagnetic field lines, illustrated by four red curves, thread the vortex from equator to middle latitudes. The magnetic field in the magnetosheath, represented by two blue curves, is dominantly northward, with slightly nightward bending in the middle latitude.

[29] The angle between the bulk velocity and the magnetic field is nearly 90° on the equatorial plane, and it increases continuously from the equator to middle latitude planes. The shear angle of the magnetic field in magnetosheath and magnetosphere increases simultaneously. These two factors lead to a weak perturbation on $Z = 8$ R_E plane (also shown in Figure 3), which is obvious from the density contours, the flow arrows, and the magnetopause boundary.

[30] Four red geomagnetic field lines, distributing on the leading and trailing edges of one vortex, align the vortices in the three planes; it is evident that the geomagnetic field controls the global structure of the nonlinear KHW. The phase evolution studied in the previous section is one representation of the alignment feature: the nightward bending of the geomagnetic field lines in the dayside induces the phase leading of the waveforms in middle latitude, while the sunward bending in the nightside generates the phase
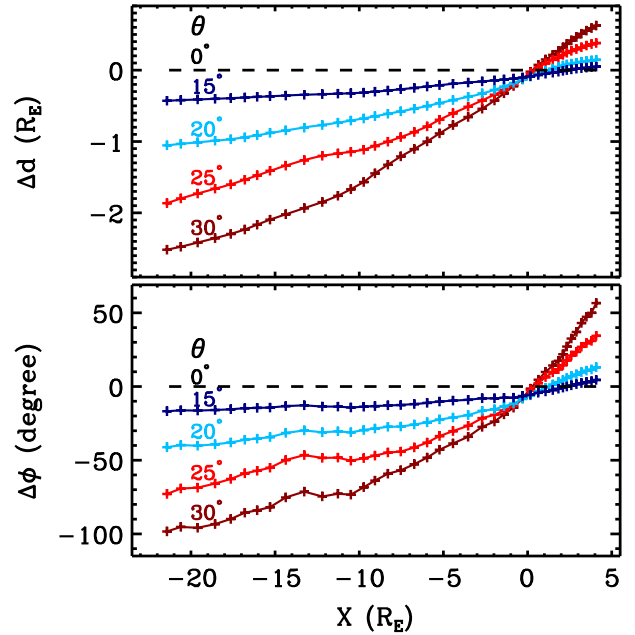
Figure 6. Distribution of waveform displacement $\triangle d$ (upper) and KHW phase difference $\triangle\phi$ (bottom) along the X direction of 15° (blue), 20° (pale blue), 25° (red), and 30° (dark red) θ planes. The computing method is introduced in the text.
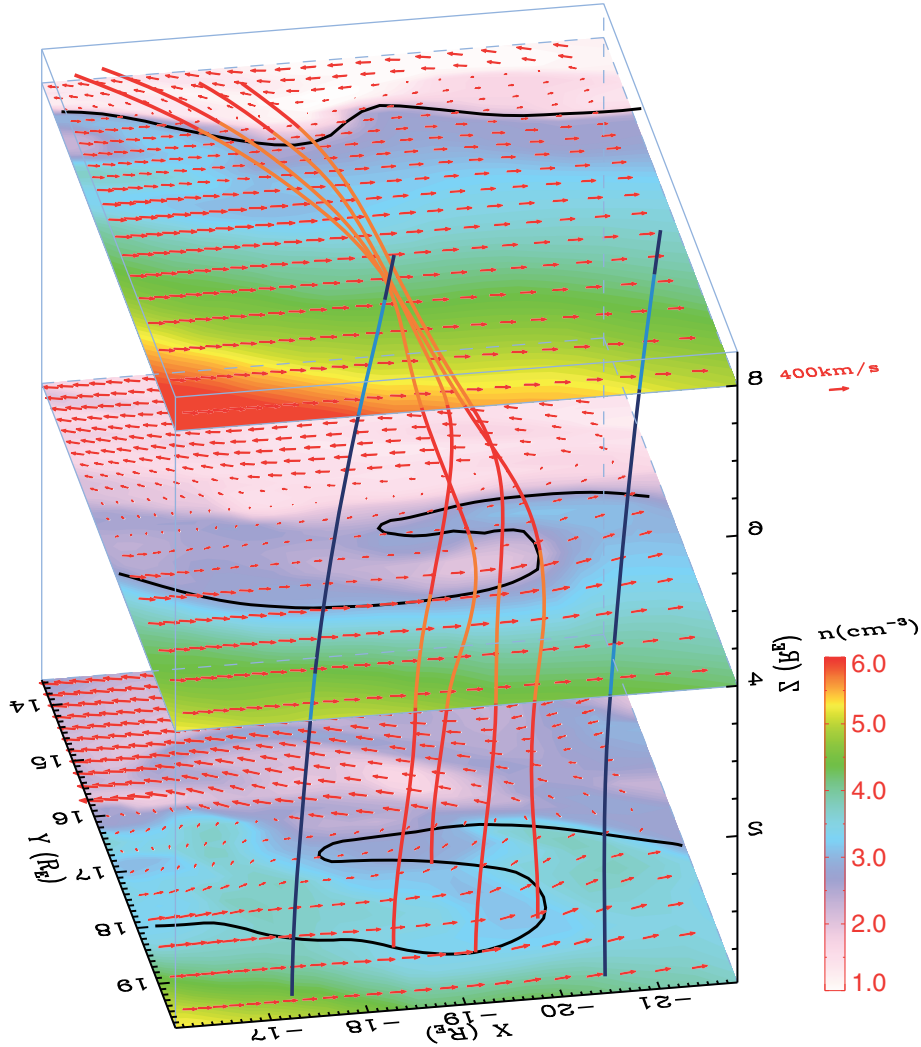
Figure 7. 3-D snapshot of the nightside low-latitude boundary layer showing the vortex orients along the geomagnetic field lines. The plasma number density is displayed by colored contours in the three planes with $Z = 0$, 4, and 8 R_E, while the tangential bulk velocities are illustrated in red arrows. The coordinate is frame shifted to a wave one, with a shift velocity about [–390, 130, 0 km/s]. One black curve in each plane is the magnetopause boundary. The magnetic fields in magnetosphere and magnetosheath are illustrated by four red curves and two blue curves, respectively.

lagging. Figure 8 shows a schematic based on the KHW global features at the magnetopause boundary layer during a pure northward IMF condition. Three curves represent the KHW active magnetopause boundary, and the curves with arrows are the geomagnetic field lines generally from dayside to nightside magnetosphere. The colored dots illustrate the KHW perturbation amplitudes, following a general color scale of Figure 3. The geomagnetic field lines align the color dots from equator to middle latitude.

[31] The 3-D or global simulation of the KHW has seldom been reported; one such study by *Gratton et al.* [2009] used 3-D large eddy simulations to study the nonlinear evolution of the vorticity. Figure 12 in their paper showed a clear evidence of the strong influence of the magnetic field direction on the formation and shape of the nonlinear features. Besides, the alignment feature is also visible in a three-dimensional view of the field lines threading one K-H vortex by *Takagi et al.* [2006], while the feature was not real-

ized in their study. One consequence of the alignment feature is the derivation of the wavelike magnetopause normal by K-H instability tends to be in field perpendicular direction, which has been represented in a Time History of Events and Macroscale Interactions during Substorms (THEMIS) statistical study by *Plaschke et al.* [2009]. A proof of the small angle between the KHW vorticity and background magnetic field is another feasible way to demonstrate the alignment feature by spacecraft observations. The work requires simultaneous measurement of four in situ spacecrafts [*Shen et al.*, 2012] and will be carried out by the future NASA Magnetospheric Multiscale Mission [*Sharma and Curtis*, 2005].

[32] The alignment feature of vortex and geomagnetic field lines brings a global structure of linear/nonlinear KHW on the magnetopause boundary and helps to propose a reasonable model of magnetic field topology within one vortex and where the reconnection could occur in association with
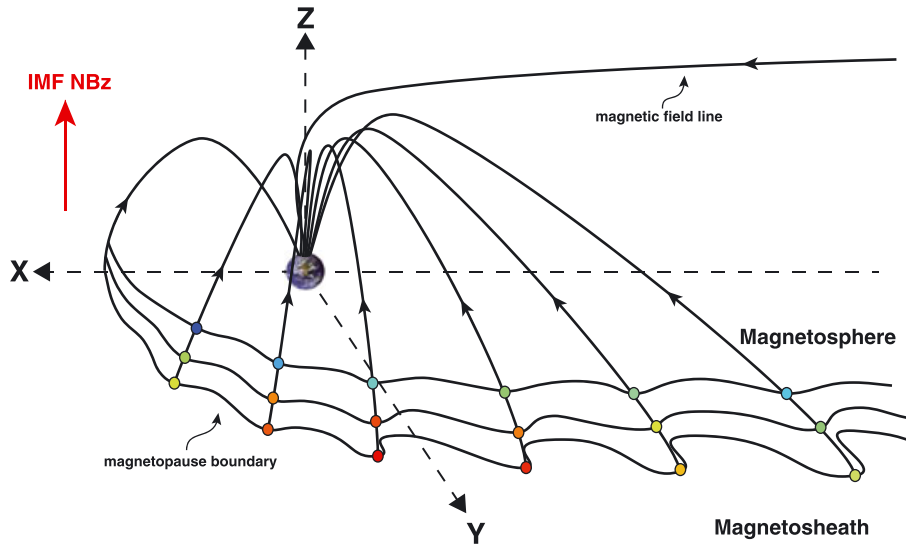
Figure 8. Schematic of global KHW at Earth's low-latitude magnetopause during the northward IMF conditions. Three curves represent the wavelike magnetopause boundary under KHW activation, and curves with arrows are the magnetic field lines of magnetosphere. The colored dots illustrate the perturbation amplitude of KHW, using a colorbar of Figure 3 generally. The geomagnetic field lines align the vortices from equator to middle latitude.

evolution of KHW. We suggest that the global perturbation distribution and alignment features are fundamental characters of KHW at the boundary layer of flow-sheared plasmas, and they may also exist on Mercury's [*Slavin et al.*, 2008], Saturn's [*Walker et al.*, 2011], and heliospheric [*Wang and Belcher*, 1998] boundaries.

[33] As shown in Figure 7, the geomagnetic fields distort and twist in the vortices and it is not strictly true that the geomagnetic field threads exactly the same phase of vortices from the equatorial to middle latitude planes. The alignment feature should be understood as the vortex's axis is controlled by geomagnetic fields. Furthermore, the feature happens when the magnetic field and bulk flow are quasi-perpendicular, and the axis of vortex may be normal to the magnetic field in a two-dimensional study of a quasi-parallel condition [*Nykyri and Otto*, 2001]. A 3-D configuration of the quasi-parallel case requires a global study during dawnward/duskward IMF, under which the KHW unstable ribbon is not embedded on the LLBL [*Farrugia et al.*, 1998; *Hwang et al.*, 2012].

5. Summary

[34] We study the global features of the Kelvin-Helmholtz waves in the low-latitude magnetopause for constant northward IMF, by means of the PPMLR-MHD global simulation model, and a new schematic of global KHW is displayed in Figure 8. The main results of this study are summarized as follows:

[35] 1. The magnetopause boundary layer is found to be widely KHW active under northward IMF. The perturbation amplitude is represented by V_X root-integrated power (*RIP*), which is computed by a spectral analysis technique.

[36] 2. The V_X *RIP* weakens gradually from the equatorial to middle latitude planes, which is probably due to the magnetic tensor force from the nonperpendicular configura-

tion of flow and sheared magnetic fields at the boundary. The latitudinal extent of the magnetopause mode KHW is much broader than that of the inner one.

[37] 3. A global KHW active region is pieced together from cuts through 14 *Y-Z* planes, and its dayside shape is consistent with the unstable region predicted by previous numerical calculation [*Farrugia et al.*, 1998; *Foullon et al.*, 2008]. The expected maximal growth rates at the dawn/dusk region result in the peak perturbation amplitude.

[38] 4. From the detailed analysis of K-H waveforms, we find that the phase along the propagation direction of KHW in middle latitude plane is leading of that in equator in the dayside magnetopause and lagging behind in the nightside. The transition locates near the dawn/dusk terminator region.

[39] 5. The phase evolution is a representation of the vortex-geomagnetic field alignment feature, which implies that the global shape of KHW is controlled by the geomagnetic field lines. The global features of amplitude distribution and vortex-geomagnetic field alignment may be common in other KHW active boundaries of flow-sheared plasmas, e.g., Mercury's magnetopause and heliopause.

References

Chandrasekhar, S. (1961), *Hydrodynamic and Hydromagnetic Stability*, Oxford Univ. Press, New York.

Claudepierre, S. G., S. R. Elkington, and M. Wiltberger (2008), Solar wind driving of magnetospheric ULF waves: Pulsations driven by velocity shear at the magnetopause, *J. Geophys. Res.*, *113*, A05218, doi:10.1029/2007JA012890.

Claudepierre, S. G., M. K. Hudson, W. Lotko, J. G. Lyon, and R. E. Denton (2010), Solar wind driving of magnetospheric ULF waves: Field line resonances driven by dynamic pressure fluctuations, *J. Geophys. Res.*, *115*, A11202, doi:10.1029/2010JA015399.

Colella, P., and P. Woodward (1984), The piecewise parabolic method (PPM) for gas-dynamical simulations, *J. Comput. Phys.*, *54*(1), 174–201, doi:10.1016/0021-9991(84)90143-8.

Cowee, M. M., D. Winske, and S. P. Gary (2010), Hybrid simulations of plasma transport by Kelvin-Helmholtz instability at the magnetopause: Density variations and magnetic shear, *J. Geophys. Res.*, *115*, A06214, doi:10.1029/2009JA015011.

Dai, W., and P. R. Woodward (1995), A simple Riemann solver and high-order Godunov schemes for hyperbolic systems of conservation laws, *J. Comput. Phys.*, *121*(1), 51–65, doi:10.1006/jcph.1995.1178.

Fairfield, D. H., A. Otto, T. Mukai, S. Kokubun, R. P. Lepping, J. T. Steinberg, A. J. Lazarus, and T. Yamamoto (2000), Geotail observations of the Kelvin-Helmholtz instability at the equatorial magnetotail boundary for parallel northward fields, *J. Geophys. Res.*, *105*(A9), 21,159–21,173, doi:10.1029/1999JA000316.

Farrugia, C. J., F. T. Gratton, L. Bender, H. K. Biernat, N. V. Erkaev, J. M. Quinn, R. B. Torbert, and V. Dennisenko (1998), Charts of joint Helvin-Helmholtz and Rayleigh-Taylor instabilities on the dayside magnetopause for strongly northward interplanetary magnetic field, *J. Geophys. Res.*, *103*(A4), 6703–6727, doi:10.1029/97JA03248.

Foullon, C., C. J. Farrugia, A. N. Fazakerley, C. J. Owen, F. T. Gratton, and R. B. Torbert (2008), Evolution of Kelvin-Helmholtz activity on the dusk flank magnetopause, *J. Geophys. Res.*, *113*, A11203, doi:10.1029/2008JA013175.

Godunov, S. (1959), A difference method for numerical calculation of discontinuous solutions of the equations of hydrodynamics, *Mat. Sbornik*, *89*(3), 271–306.

Gratton, F. T., L. E. Bilbao, C. J. Farrugia, and G. Gnavi (2009), Large eddy simulations in MHD: The rise of counter-rotating vortices at the magnetopause, *J. Phys. Conf. Ser.*, *166*(1), 012023 pp., doi:10.1088/1742-6596/166/1/012023.

Guo, X., C. Wang, and Y. Hu (2010), Global MHD simulation of the Kelvin-Helmholtz instability at the magnetopause for northward interplanetary magnetic field, *J. Geophys. Res.*, *115*, A10218, doi:10.1029/2009JA015193.

Guo, X. C., C. Wang, T. R. Sun, and Y. Q. Hu (2011), Shock waves standing in the middle- and high-latitude magnetosheath from global MHD simulations, *J. Geophys. Res.*, *116*, A03206, doi:10.1029/2010JA016268.

Hasegawa, H., M. Fujimoto, T. D. Phan, H. Reme, A. Balogh, M. W. Dunlop, C. Hashimoto, and R. TanDokoro (2004), Transport of solar wind into Earth's magnetosphere through rolled-up Kelvin-Helmholtz vortices, *Nature*, *430*(7001), 755–758, doi:10.1038/nature02799.

Hasegawa, H., M. Fujimoto, K. Takagi, Y. Saito, T. Mukai, and H. Reme (2006), Single-spacecraft detection of rolled-up Kelvin-Helmholtz vortices at the flank magnetopause, *J. Geophys. Res.*, *111*, A09203, doi:10.1029/2006JA011728.

Hasegawa, H., et al. (2009), Kelvin-Helmholtz waves at the Earth's magnetopause: Multiscale development and associated reconnection, *J. Geophys. Res.*, *114*, A12207, doi:10.1029/2009JA014042.

Hu, Y. Q., X. C. Guo, and C. Wang (2007), On the ionospheric and reconnection potentials of the Earth: Results from global MHD simulations, *J. Geophys. Res.*, *112*, A07215, doi:10.1029/2006JA012145.

Hwang, K. J., M. L. Goldstein, M. M. Kuznetsova, Y. Wang, A. F. Viñas, and D. G. Sibeck (2012), The first in situ observation of Kelvin-Helmholtz waves at high-latitude magnetopause during strongly dawnward interplanetary magnetic field conditions, *J. Geophys. Res.*, *117*, A08233, doi:10.1029/2011JA017256.

Lai, S. H., and L. H. Lyu (2010), A simulation and theoretical study of energy transport in the event of MHD Kelvin-Helmholtz instability, *J. Geophys. Res.*, *115*, A10215, doi:10.1029/2010JA015317.

Lee, L. C., R. K. Albano, and J. R. Kan (1981), Kelvin-Helmholtz instability in the magnetopause-boundary layer region, *J. Geophys. Res.*, *86*(A1), 54–58, doi:10.1029/JA086iA01p00054.

Li, W. Y., X. C. Guo, and C. Wang (2012), Spatial distribution of Kelvin-Helmholtz instability at low-latitude boundary layer under different solar wind speed conditions, *J. Geophys. Res.*, *117*, A08230, doi:10.1029/2012JA017780.

Liu, H. L., and Z. H. Huang (2011), Size and shape of magnetopause in the noon-midnight meridian plane based on the MHD simulation, *Chin. J. Space Sci.*, *31*(1), 15–19.

Mills, K. J., A. W. Longbottom, A. N. Wright, and M. S. Ruderman (2000), Kelvin-Helmholtz instability on the magnetospheric flanks: An absolute and convective instability approach, *J. Geophys. Res.*, *105*(A12), 27,685–27,699, doi:10.1029/1999JA000289.

Miura, A. (1984), Anomalous transport by magnetohydrodynamic Kelvin-Helmholtz instabilities in the solar-wind magnetosphere interaction, *J. Geophys. Res.*, *89*(A2), 801–818, doi:10.1029/JA089iA02p00801.

Miura, A. (1992), Kelvin-Helmholtz instability at the magnetospheric boundary: Dependence on the magnetosheath sonic mach number, *J. Geophys. Res.*, *97*(A7), 10,655–10,675, doi:10.1029/92JA00791.

Miura, A. (1995), Dependence of the magnetopause Kelvin-Helmholtz instability on the orientation of the magnetosheath magnetic field, *Geophys. Res. Lett.*, *22*(21), 2993–2996, doi:10.1029/95GL02793.

Nykyri, K., and A. Otto (2001), Plasma transport at the magnetospheric boundary due to reconnection in Kelvin-Helmholtz vortices, *Geophys. Res. Lett.*, *28*(18), 3565–3568, doi:10.1029/2001GL013239.

Paschmann, G., and P. W. Daly (1998), *Analysis Methods for Multi-Spacecraft Data*, International Space Science Institute, ESA Publications Divisions, Noordwijk, The Netherlands.

Plaschke, F., et al. (2009), Statistical study of the magnetopause motion: First results from THEMIS, *J. Geophys. Res.*, *114*, A00C10, doi:10.1029/2008JA013423.

Pu, Z. Y., and M. G. Kivelson (1983), Kelvin-Helmholtz instability at the magnetopause: Energy flux into the magnetosphere, *J. Geophys. Res.*, *88*(A2), 853–861, doi:10.1029/JA088iA02p00853.

Sckopke, N., G. Paschmann, G. Haerendel, B. U. O. Sonnerup, S. J. Bame, T. G. Forbes, E. W. Hones, and C. T. Russell (1981), Structure of the low-latitude boundary layer, *J. Geophys. Res.*, *86*(A4), 2099–2110, doi:10.1029/JA086iA04p02099.

Sharma, A. S., and S. A. Curtis (2005), Magnetospheric multiscale mission, in *Nonequilibrium Phenomena in Plasmas, Astrophysics and Space Science Library,* vol. 321, edited by W. B. Burton et al., pp. 179–195, Springer, Netherlands.

Shen, C., et al. (2012), Spatial gradients from irregular, multiple-point spacecraft configurations, *J. Geophys. Res.*, *117*, A11207, doi:10.1029/2012JA018075.

Slavin, J., et al. (2008), Mercury's magnetosphere after MESSENGER's first flyby, *Science*, *321*(5885), 85–89, doi:10.1126/science.1159040.

Sonnerup, B. U. O. (1980), Theory of the low-latitude boundary layer, *J. Geophys. Res.*, *85*(A5), 2017–2026, doi:10.1029/JA085iA05p02017.

Spreiter, J., A. Summers, and A. Alksne (1966), Hydromagnetic flow around the magnetosphere, *Planet. Space Sci.*, *14*(3), 223–253, doi:10.1016/0032-0633(66)90124-3.

Takagi, K., C. Hashimoto, H. Hasegawa, M. Fujimoto, and R. Tan-Dokoro (2006), Kelvin-Helmholtz instability in a magnetotail flank-like geometry: Three-dimensional MHD simulations, *J. Geophys. Res.*, *111*, A08202, doi:10.1029/2006JA011631.

Taylor, M. G. G. T., et al. (2012), Spatial distribution of rolled up Kelvin-Helmholtz vortices at Earth's dayside and flank magnetopause, *Ann. Geophys.*, *30*(6), 1025–1035, doi:10.5194/angeo-30-1025-2012.

Terasawa, T., et al. (1997), Solar wind control of density and temperature in the near-Earth plasma sheet: WIND/GEOTAIL collaboration, *Geophys. Res. Lett.*, *24*(8), 935–938, doi:10.1029/96gl04018.

Thomson, D. J. (1982), Spectrum estimation and harmonic analysis, *Proc. IEEE*, *70*(9), 1055–1096, doi:10.1109/PROC.1982.12433.

Walker, A. D. M. (1981), The Kelvin-Helmholtz instability in the low-latitude boundary layer, *Planet. Space Sci.*, *29*(10), 1119–1133, doi:10.1016/0032-0633(81)90011-8.

Walker, R. J., K. Fukazawa, T. Ogino, and D. Morozoff (2011), A simulation study of Kelvin-Helmholtz waves at Saturn's magnetopause, *J. Geophys. Res.*, *116*, A03203, doi:10.1029/2010JA015905.

Wang, C., and J. W. Belcher (1998), Numerical investigation of hydrodynamic instabilities of the heliopause, *J. Geophys. Res.*, *103*(A1), 247–256, doi:10.1029/97JA02773.